Topographic modifications to bottom Ekman layer structure

Isaiah Cuadras, James C. McWilliams, and Marcelo Chamecki
Department of Atmospheric and Oceanic Sciences,
University of California, Los Angeles, California 90095, USA

(Received 26 November 2024; accepted 22 April 2025; published 19 May 2025)

A bottom Ekman layer is defined by a dynamic balance between the Coriolis force, pressure gradient force, and turbulent transport. We investigate how this balance is modified by bottom topography by analyzing Large Eddy Simulations of separating flow over a two-dimensional ridge. The focus is on two cases that include rotation: one where the exterior flow is driven across the ridge (Cross-Hill with Rotation: "CHR"), and another where the flow is driven along the ridge axis (Along-Hill with Rotation: "AHR"). In both cases, the bottom portion of the boundary layer is dominated by topographic disturbances, including a speedup over the hill and a recirculation in the wake. While these near-bottom modifications are rooted in nonrotating flow dynamics (evidenced in nonrotating simulations presented here), they are impacted by the Coriolis force, leading to a wake jet in the along-ridge flow component of CHR and a wake deficit in the along-ridge component of AHR. These features drive magnifications in the ageostrophic transport that cannot be predicted by the bottom stress. Analysis of the transport budget suggests the wake dynamics are sensitive to the strength of the horizontal divergence of the Reynold's stresses, being stronger in CHR than in AHR. This leads to a large nonlocal influence in CHR, where averaging the ageostrophic transport over a distance that is 3 times the hill's total length leads to a more than 30% increase in magnitude when compared to the flat case. Averaging over the same distance in AHR shows negligible differences to the bulk transport relative to the flat case, as the wake is more confined to the topography vicinity. These results show that the influence of rotation on the speedup and recirculation play an essential role in facilitating topographically induced changes to the bulk transport, with an evident dependence on the strength of flow separation.

DOI: 10.1103/PhysRevFluids.10.053802

I. INTRODUCTION

Planetary fluids are often characterized by an approximate dynamical balance between the Coriolis force and a transverse pressure gradient, termed geostrophic balance. One instance in which geostrophic balance can be broken is in the presence of a physical boundary, such as the bottom of the atmosphere or the top and bottom of the ocean. Assuming an f-plane approximation (and neglecting effects from buoyancy and molecular viscosity) gives the following form of the incompressible momentum equation governing geophysical flows:

$$\frac{\partial \boldsymbol{u}}{\partial t} + \boldsymbol{u} \cdot \nabla \boldsymbol{u} = -\frac{1}{\rho_0} \nabla p + f \boldsymbol{e}_3 \times \boldsymbol{u}, \tag{1}$$

where $\boldsymbol{u}$ is the velocity vector, ρ_0 is the reference density, f is the Coriolis parameter, and p is pressure. Boldface variables are vector valued, where $\boldsymbol{e}_3$ is the unit vector in the vertical direction. Geostrophic balance retains only the first and third terms on the right-hand side of Eq. (1), i.e.,

$$f \boldsymbol{e}_3 \times \boldsymbol{u}_g = \frac{1}{\rho_0} \nabla p, \tag{2}$$

where $\boldsymbol{u}_g$ is the "geostrophic" velocity. If we consider a steady in-time flow that is horizontally homogeneous and assume that the boundary-layer pressure is equivalent to the external flow pressure, we can ensemble average Eq. (1) to get

$$f\boldsymbol{e}_3 \times (\langle \boldsymbol{u} \rangle - \boldsymbol{u}_g) = -\frac{\partial \langle \boldsymbol{u}' w' \rangle}{\partial z}. \tag{3}$$

Here we have rewritten the pressure gradient as $f\overline{\boldsymbol{u}}_g$ from Eq. (2), and the last term is the vertical divergence of the Reynolds stresses, representing the influence of the turbulent momentum fluxes. Angle brackets $\langle \cdot \rangle$ indicate ensemble averages, while primes $(')$ indicate fluctuations around the mean state.

The result of Eq. (3) is a mean velocity vector that changes direction with distance from the boundary, the so-called Ekman layer. Ekman layers have been given substantial attention and are relatively well understood, especially in the context of the assumptions in Eq. (3). Their foundations reside in idealized theoretical approaches, where a constant-value eddy viscosity assumption can be invoked as a method for turbulence closure [1]. From this, the well-known Ekman spiral structure can be predicted, giving an estimate for the shape and magnitudes of the velocity profiles. The Use of Direct Numerical Simulations and Large Eddy Simulations (LES) has validated and refined early theoretical predictions of the Ekman layer, leading to more elaborate descriptions of the associated dynamics (e.g., [2–4]).

An aspect of the Ekman layer that is of particular importance in the ocean is the resulting "Ekman transport." Vertically integrating the balance in Eq. (3) leads to

$$U_a \equiv \int_0^\delta (\langle u \rangle - u_g) dz = \langle \tau_{yz} \rangle / f, \tag{4}$$

$$V_a \equiv \int_0^\delta (\langle v \rangle - v_g) dz = -\langle \tau_{xz} \rangle / f, \tag{5}$$

where the vertical integral of $\langle \boldsymbol{u} \rangle - \boldsymbol{u_g}$ defines the Ekman (or ageostrophic) transport $\boldsymbol{U}_a$, δ is the height of the boundary layer, and $\langle \tau_{xz} \rangle$ and $\langle \tau_{yz} \rangle$ are the components of the bottom stress. This also holds for an idealized ocean surface, although we focus our attention here on bottom Ekman layers. The theoretical result is that the Ekman transport can be predicted exactly by the bottom stress and local magnitude of the earth's rotation, making Eqs. (4) and (5) independent of any turbulence closure model. Throughout the paper, we will refer to a flow that satisfies Eqs. (3)–(5) as being in an "Ekman balance."

Understanding the dynamics of Ekman transport is important due to its effect on the distribution of material ocean properties, such as nutrients, temperature, salinity, and pollutants [5–7]. To this end, studies have sought to validate Eqs. (3)–(5) in the field with varying levels of agreement. For example, [8] reported decent near-bottom agreement of a measured Ekman spiral with theoretical predictions, although data suggested overprediction of the transport near the pycnocline. This is in contrast to measurements in [9] and numerical simulations in [10] that suggest most of the Ekman transport is confined to the bottom mixed layer, having only small contributions near the pycnocline, although discrepancies between the studies may be explained by differing stratification strengths. Measurements in the East Australian Current system have also attempted to quantify the bottom ocean transport, capturing around 60%–70% of the variability with Eqs. (4) and (5) [11,12]. It was proposed that part of the disagreement could be associated with local bottom topography, although the spatial resolution of bottom current measurements is still too coarse to investigate this influence in the field. A numerical model of the same region showed that the area-averaged bottom stress played a small role in the overall transport budget, with larger contributions coming from nonlinear advection and bottom pressure variations [13].

The flat-bottom assumption inherent to Eqs. (3)–(5) is invalid in many places in the atmosphere and ocean (e.g., in the presence of topography). It is then of little surprise that associated transport predictions have proven imperfect in the field since there is likely a strong influence from bottom topography. Literature in the atmospheric boundary layer and engineering communities have investigated the influence of topography in boundary layers without rotational effects. For example, early work showed that the velocity in a boundary layer can increase in magnitude in the neighborhood of topography, quantifying the velocity "speedup" over hills with gentle slopes by way of linear approximations [14,15]. The speedup is driven by the fact that the topography imposes a spatial constraint on the boundary layer height, forcing a convergence of mean streamlines in its vicinity [16]. Experimental and numerical studies have shown good agreement of speedup values with the gentle-slope theory [17,18], lending confidence to our understanding of shallow topography's influence on boundary layer flow. Despite the success of [14] and [15], the negligence of nonlinearities is no longer valid once the slope becomes large, making their predictions inappropriate for large-slope regimes [19].

Advances in the respect of large-slope topographies have been made primarily by laboratory experiments and numerical simulations. The flow in a turbulent boundary layer with steady statistics and steep topography is governed by a balance between turbulent transport, mean advection, and the associated pressure gradient. Early experiments showed that an adverse pressure gradient can develop when curvature effects are large [20,21]. Boundary-layer separation can then occur as a consequence if the adverse pressure gradient is large enough, leading to a near-bottom flow that reverses direction in the wake of the topography [22,23]. This is the essence of a "separation bubble," generally being identifiable by a time-mean recirculation pattern in the wake with a stream function that is opposite in sign to the exterior flow. Numerical simulations have shown that the conditions for flow separation over two-dimensional and three-dimensional obstacles are controlled by the bottom roughness (z_0), upstream velocity characteristics, and topography slope [24,25]. Here, z_0 is an empirical estimate for the length scale of topographic irregularities, often used as a means for approximating the wall stress via the logarithmic law of the wall. The presence of a separation bubble has an influence on the streamwise velocity that is similar to the effect of the topography, that is, the separation bubble serves as an additional constraint on the pathways upstream fluid particles can take, leading to a sustained speedup above its vicinity [26].

Research on the combined presence of rotation and topography seems relatively sparse. Early work was motivated by the need for better parametrization of drag in numerical weather prediction models [27,28], although it was deemed that the influence of rotation on bulk drag was minimal when flow separation was prevalent. Since then the focus appears to have shifted toward analyzing the influence of rotation on the structure of isolated and suspended wakes. For example, attention has been given to the stabilizing influence of rotation, where it has been shown to suppress turbulent motions [29,30]. A recent study quantified this influence by identifying the Reynolds number necessary for inducing flow separation at a variety of Rossby number regimes [31]. Studies motivated by wind energy extraction have considered the joint presence of rotation and flow separation [32,33], although such studies are not readily generalized to bottom irregularities.

In this paper, we seek to understand the influence topography has on the structure of an Ekman layer and the associated boundary layer transport, where present simulations are most representative of shallow ocean conditions without surface forcing. We begin by describing our methods in Sec. II, detailing both the numerical implementation and the physical configuration. We follow this in Sec. III in three parts, first by discussing modifications to the boundary layer structure, followed by an analysis of the transport balance, and lastly with a brief discussion on the role of nonrotating dynamics. Section IV concludes the paper with a summary of the presented results.

II. METHODS

A. Numerics

We solve the three-dimensional uniform density, incompressible, Navier-Stokes equations with a LES model to investigate the problem:

$$\nabla \cdot \tilde{\boldsymbol{u}} = 0, \tag{6}$$

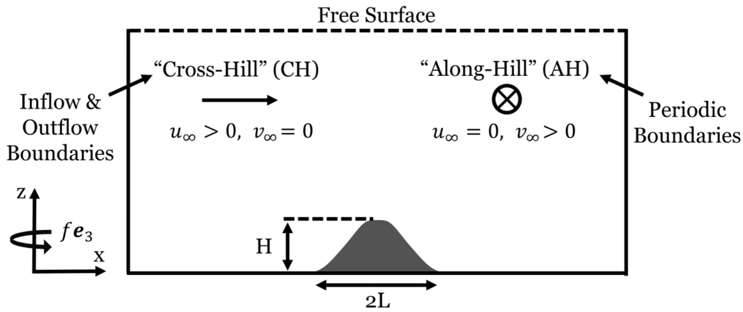

FIG. 1. General configuration of the simulations present in this study. Note the dependence of the boundary conditions on the free-stream velocity orientation. See Table I for a description of the simulated cases and their acronyms (CH, AH, etc.).

$$\frac{\partial \tilde{\boldsymbol{u}}}{\partial t} + \tilde{\boldsymbol{u}} \cdot \nabla \tilde{\boldsymbol{u}} = -\frac{1}{\rho_0}\nabla \tilde{p}_a + f\boldsymbol{e}_3 \times \tilde{\boldsymbol{u}} - \nabla \cdot \boldsymbol{\tau}^{\mathrm{SGS}} + \boldsymbol{\Pi} + \boldsymbol{F}_{\mathrm{IBM}}. \tag{7}$$

Since LES does not capture the smallest scales of turbulence, a grid filter is required to separate the resolved scales (indicated by a tilde) from the subgrid scales (SGS) [34]. In the above equations, $\tilde{\boldsymbol{u}}$ represents the three-dimensional velocity field, $\tilde{p}_a$ represents pressure anomalies, $\boldsymbol{\tau}^{\mathrm{SGS}}$ is the deviatoric part of the SGS stress tensor, $\boldsymbol{\Pi}$ is an imposed pressure gradient force, and $\boldsymbol{F}_{\mathrm{IBM}}$ is a force imposed to satisfy the boundary conditions of the topography using the Immersed Boundary Method (IBM). In the cases where there is rotation, we prescribe a domain-uniform pressure gradient force of $\boldsymbol{\Pi} = -f\boldsymbol{e_3} \times \boldsymbol{u}_g$, following Eq. (2). Otherwise, $\boldsymbol{\Pi}$ is chosen to obtain a far-field velocity that is close in value to those in the cases with rotation (see Sec. II B for more). The figures in the following sections display the sum of resolved and SGS quantities (unless otherwise noted), and therefore forgo the tilde and SGS superscripts.

The topography is represented on a Cartesian grid following the IBM [35]. In particular, the discrete forcing method is used to compute $\boldsymbol{F}_{\mathrm{IBM}}$ in Eq. (7) to force the velocity field inside the topography to zero (see the Appendix of [36] for more). The combined use of the IBM and spectral derivatives is notorious for producing spurious oscillations in computed flow quantities due to the discontinuity introduced by the topography, often called the Gibbs phenomenon [37]. We employ a cubic interpolation to minimize the artifices introduced by the Gibbs phenomenon [38]. We further smooth the output variables shown in Sec. III B for added interpretability, although this does not alter any of the primary conclusions. Validation of the present IBM model used can be found in the Appendix of [39].

Horizontal derivatives are computed using pseudospectral methods and laterally periodic boundary conditions, while vertical derivatives are computed on a second-order accurate staggered grid using the central-difference method. A scale-dependent Smagorinsky model is used to dynamically compute $\boldsymbol{\tau}^{\mathrm{SGS}}$ via Lagrangian averaging [34].

B. Simulation design

The domain configuration, depicted in Fig. 1, features a two-dimensional topography shape in the xz plane. The horizontal periodicity results in a topography of infinite span in the y direction, akin to an oceanic ridge or atmospheric mountain range. We interchangeably use the word "hill" throughout the paper to describe the topography, recognizing that hills are generally not restricted to two-dimensional shapes. We maintain an identical topographic shape throughout all simulations (excluding the flat control cases), characterized by a maximum slope of $\theta_{\max} \approx 44^\circ$ and an aspect ratio of $H/L \approx 0.57$, steeper than typical oceanic topography. This particular geometry was chosen

TABLE I. A table showing the simulations presented in this paper containing topography. The prefix "CH" is for Cross-Hill, while the prefix "AH" is for Along-Hill. Labels ending in "R" indicate rotational influence, while labels ending in "NR" indicate no rotational influence. Flat-bottom control cases were also simulated using configurations that are identical to those below.

Case	u_∞/u_*	v_∞/u_*	TKE_∞/u_*^2	f (s^{-1})	$L_x/H\times L_y/H\times L_z/H$	$N_x\times N_y\times N_z$
CHR	14	0	1.1	10^{-4}	$24\times12\times4.8$	$384\times192\times192$
AHR	0	13	1.1	10^{-4}	$18\times12\times4.8$	$288\times192\times192$
CHNR	17	0	2.3	0	$24\times12\times4.8$	$384\times192\times192$
AHNR	0	17	2.3	0	$18\times12\times4.8$	$288\times192\times192$

due to its comprehensive documentation [40] and its susceptibility to flow separation. Its shape is defined by a piecewise continuous function that is designed to quickly transition to a steep slope (see [26] and the corresponding database for more details). We anticipate that flow separation will lead to a stronger disturbance to the canonical Ekman boundary layer balance, allowing for a more demanding appraisal of Eqs. (3)–(5).

Simulations are classed either as "Cross-Hill" (CH) or "Along-Hill" (AH) based on the orientation of the far-field flow (Table I). Cases both with rotation (R) and without rotation (NR) are simulated, along with their flat counterparts for comparison. Simulations containing rotation use a constant Coriolis parameter of $f = 10^{-4}$ s^{-1}, giving a Rossby number of Ro ≈ 30 ($\text{Ro} = u_g/fL$), representative of small-scale bottom topography. Due to the homogeneity in the y direction, our average quantities (indicated by overbars) consist both of a spatial average in the y direction and a time average, where the time-averaging window is chosen to be an integer multiple of an inertial period for cases with rotation. We prescribe a free-surface upper boundary condition, resembling an ocean with no surface forcing. The bottom of the domain is a no-slip boundary with a bottom roughness of $z_o = 10$ cm, a value that is around 2–10 times larger than typical shallow water conditions [41]. We use z_o only as a means for computing the wall stress via an assumed logarithmic mean velocity profile and do not anticipate significant influence on the overall flow field. We assume a field of constant density throughout all cases and thus do not consider any influences from buoyancy.

The far-field flow components, u_∞ and v_∞, are the mean u and v components of velocity at the top of the domain near the horizontal boundary. Table I shows their values, normalized by the bottom friction velocity ($u_* = \sqrt{\tau_b/\rho_0}$) at the same x/H location, rounded to the nearest integer. The τ_b used in calculating u_* is the magnitude of the bottom stress as $\tau_b = \sqrt{\tau_{xz}^2 + \tau_{yz}^2}$. CHNR and AHNR have slightly more energetic far-field flows when compared to CHR and AHR. This is because the Coriolis force introduces a constraint on the height of the boundary layer that scales with u_*/f [42], whereas the boundary layer in cases without rotation grows without bound (albeit, a relatively slow growth). For instance, we can take a Reynolds number that scales with the boundary layer height as Re $\sim U\delta/\nu$, where ν is the kinematic viscosity and U is the magnitude of the far-field flow ($U = \sqrt{u_\infty^2 + v_\infty^2}$). For a rotating, flat-bottom boundary layer, we can use the fact that $\delta \sim u_*/f$ to rewrite this as $u_* \sim \nu f \text{Re}/U$. In contrast, it can be shown that nonrotating, flat-bottom boundary layers have the scaling relationship $u_* \sim \rho U\delta/D \sim \nu\text{Re}/D$, where D is a characteristic horizontal length scale [43]. Taking the ratio yields $u_*^{NR}/u_*^R \sim U/(fD)$. For a constant value of U, the ratio of the far-field friction velocities is then controlled by the ratio of a rotational timescale to an advective timescale. From this perspective, we can expect that, for large D, $u_*^{\text{R}} > u_*^{\text{NR}}$ since an advective timescale will become longer than the present rotational timescale. We emphasize that the scaling of the friction velocity ratio with $U/(fD)$ is not directly related to the Rossby number since we are drawing a comparison across two separate cases, as opposed to evaluating the scales of a single problem.

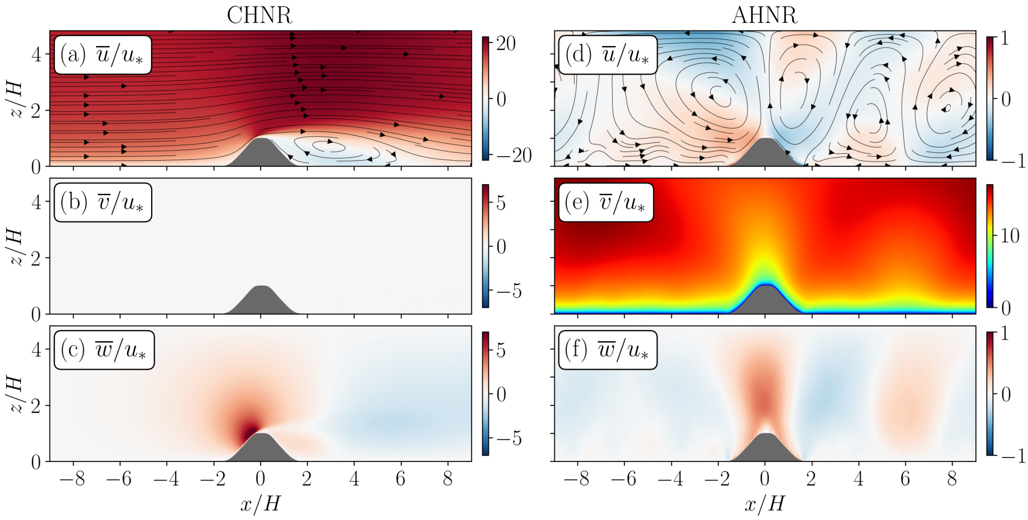

FIG. 2. Lateral ($\overline{u}, \overline{v}$) and vertical ($\overline{w}$) velocities normalized by a far-field friction velocity u_* for the nonrotating cases ($f = 0$). The left panels are for CHNR, while the right panels are for AHNR. The lines overlaying the top row are mean streamlines [defined by Eq. (12) when $u_g = 0$].

Nonlocal effects from the wake are strong in the CH cases. This is problematic when combined with the use of periodic boundary conditions, as the downstream flow then propagates through the outlet, eventually contaminating the impinging flow characteristics. We seek to study a case where the impinging flow is that of a flat boundary layer, and thus prescribe an inflow condition to remedy this effect. In essence, this consists of running a precursor simulation with a flat bottom and then using its result to force the upstream flow in the simulation with topography. At the outlet, we transition the flow from the simulation with topography to the flow conditions from the flat cases. This transition takes place over the last one-sixth of the domain length and is defined by a cosine function that sharply cuts off after 75% of the smoothing region (see [44] for more details). We do this only for the CH cases, as separation effects in the AH cases were weak enough to recover a far-field momentum balance that closely resembles that of a flat Ekman boundary layer. The cases with prescribed inflow conditions required larger domains so that the downstream flow field could smoothly transition to the inflow condition in order to satisfy the periodicity. The pressure perturbation introduced by the topography also had a notable enough upstream influence such that cases with a prescribed inflow required a small spatial distance to adjust to the new domain. For this reason, the far-field values in Table I are defined as one hill unit from the inlet edge for CHR and CHNR. We have truncated the domains of these cases in the following figures for visualization purposes so that they appear to be of equal size to the AHR and AHNR cases. In particular, CHR and CHNR have domains of length $L_x = 24H$, although we only display the domain on the interval $[H, 19H]$.

III. RESULTS AND DISCUSSION

A. Boundary-layer structure

1. Without rotation

Figures 2(a)–2(c) show the velocity field for CHNR. This is a well-documented case, displaying typical features of a strongly separated boundary layer for flow past a two-dimensional hill. Namely, the recirculating wake and streamwise velocity speedup are apparent (upper left panel). The right panels of Figs. 2(d)–2(f) correspond to the AHNR case. Here, the secondary circulation features are far less dominant, driven by velocity components ($\overline{u}$ and $\overline{w}$) that are less than 10% the magnitude of the dominant velocity component ($\overline{v}$). We remark that the asymmetry in the recirculation of AHNR decreases with integration time and should not be present in the final, steady-state solution, though it is present here due to slow convergence of the statistics. This particular orientation has received less attention in the literature, although existing studies report similar phenomena for flows aligned with heterogeneous roughness elements [45,46]. It has been proposed that the mechanism is related to the lateral heterogeneity of drag induced by the topography. This leads to horizontal gradients in the Reynolds stresses (see [45]) that drive the $\overline{u}$ component of flow seen in Fig. 2(d). Because $\frac{\partial \overline{v}}{\partial y} = 0$ under sufficiently long time averages, a vertical flow component must be generated to satisfy the incompressibility condition [Fig. 2(f)], leading to the secondary circulation.

Both of our nonrotating simulations live at opposite extremes, where CHNR has no pressure gradient forcing imposed in the y direction, and AHNR has no pressure gradient forcing imposed in the x direction. An intermediate scenario would impose the force at a bulk angle such that both $u_\infty \neq 0$ and $v_\infty \neq 0$. While not shown here, our own simulations investigating this influence suggested that the secondary circulations present in AHNR disappear quickly for small values of u_∞ (i.e., they are highly sensitive to small angles in the far-field flow). We then neglect further evaluation of the secondary circulations present in AHNR, as they are unlikely to occur in nature when topographic slopes are large.

It is beneficial to compare the far-field flow characteristics between CHR and CHNR before proceeding. Table I shows the Turbulent Kinetic Energy ($\text{TKE} = \frac{1}{2}\overline{\boldsymbol{u}' \cdot \boldsymbol{u}'}$) from the flat precursor simulations without topography for each of the respective cases, averaged over the entire domain (defined as TKE_∞). This shows that, on average, cases without rotation are more than twice as energetic as cases with rotation. This is consistent with the scaling arguments presented in Sec. II B. Since the boundary-layer height of an Ekman layer scales as $\delta \sim u_*/f$, we can take the limiting case of no rotation as one with a comparatively deeper boundary layer than in a case with rotation. Since the boundary-layer height scales with the Reynolds number, we can expect a more turbulent layer (i.e., a higher average TKE).

The far-field turbulence in the rotating cases decays near the top of the domain so that $\delta \approx L_z$ (L_z being the domain height), while the nonrotating cases have a domain with strong TKE throughout the entire water column. We emphasize again that our simulations are meant to represent a shallow ocean with no surface forcing, consistent with a fully turbulent water column in the coastal ocean. Regional simulations have shown evidence that the role of topography on transport may be more pronounced in shallower waters [13], serving as encouragement in the applicability of the present configuration. The following results generally exist in the regime where $0 \ll H/\delta \ll 1$, with an H/δ value of 0.2 (i.e., topography with heights that are smaller than the far-field boundary-layer height).

2. With rotation

The influence of rotation in the CHR case is most evident in the appearance of an into-the-page (v) velocity component [Fig. 3(b)], as expected from the flat Ekman Layer theory. A wake jet associated with the v component of velocity develops, with a magnitude comparable to the far-field streamwise velocity. Flat Ekman boundary layers have been shown to have a low-level jet of their own in the same velocity component, with their mechanism being attributed in part to the inertial oscillations associated with the perturbation to geostrophic balance [47,48]. It has also been shown that the low-level jet in v can be magnified over a slope [49], although this was focused on the upwind side of a topography with no separation. Here, the intensification of the wake jet is largely driven by an entrainment of momentum from the separating boundary layer into the wake (as we will show in Sec. III B). Figure 3(b) also shows the wake jet maximum appears to be well aligned with the zero line of the streamwise velocity and contained primarily within the separation bubble. While the velocity structures in the left panels of Fig. 3 are otherwise quite similar to CHNR, it is worth noting that, to our knowledge, the wake jet cannot be reproduced by imposing a bulk flow angle in a case without rotation. This is because the peak near-surface velocity in the background

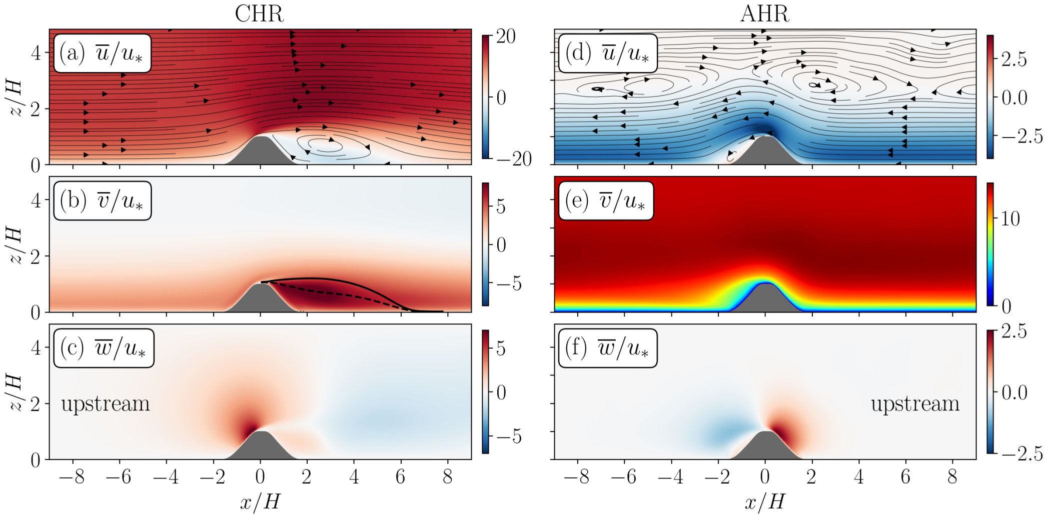

FIG. 3. As in Fig. 2, now for the rotating cases. The middle-left panel shows the isolines where the stream function (solid) and streamwise velocity (dashed) equal zero. Note that the downstream and upstream directions are opposite for the two cases, as labeled in the bottom panels.

state of CHR is higher than it is in CHNR. In other words, the velocity near the bottom in CHNR is smaller in magnitude than it is in CHR. This makes it so that when the flow above the ridge separates, the momentum of the fluid entrained by the wake is of lower magnitude in CHNR than it is in CHR.

Rotation's most notable influence in the AHR case was to diminish the domain-filling circulations that were present in AHNR [Figs. 3(d)–3(f)]. This is primarily the result of an appreciable mean velocity developing in the cross-hill direction and the resulting flow separation. With this, AHR and CHR are similar in the sense that they have far-field flows with boundary-layer velocity components in both the x and the y directions, only with differing orientations. Note that in AHR, the u component of velocity is in the opposite direction of CHR's u component. While the separation bubble in AHR is comparatively weak relative to the separation bubble in CHR (due to the u component of velocity being smaller in magnitude), the separation bubble in AHR clearly has an appreciable influence on the velocity field. For example, the along-hill component of velocity in AHR is attenuated in the wake of the topography. This is in stark contrast to CHR, where the along-hill velocity was magnified in the separation bubble. In addition, the separation bubble in CHR served to increase the u component of velocity above the shear layer ($\Delta u > 0$), acting as a constraint on the pathway of upstream fluid particles. In AHR, the cross-hill component of velocity does not experience the same level of magnification. In fact, we can see the far-field peak in the u component of velocity is larger in magnitude than the velocity above the shear layer.

Much of what controls the differences between CHR and AHR can be attributed to the nature of the separation region. To illustrate this, Fig. 4 shows the TKE, TKE production (P), and TKE dissipation (ϵ) for CHR and AHR, where P and ϵ are given by

$$P = -\overline{\boldsymbol{u}'\boldsymbol{u}'} : \nabla \overline{\boldsymbol{u}}, \tag{8}$$

$$\epsilon = -\overline{\boldsymbol{\tau}^{\mathrm{SGS}} : \boldsymbol{S}}, \tag{9}$$

with $\boldsymbol{S}$ being the strain-rate tensor. Use of $\boldsymbol{\tau}^{\mathrm{SGS}}$ in calculating the dissipation of TKE has been shown to be reliable for the present SGS model [34]. The goal is not to carry out a detailed energy budget, but to highlight some features of the present TKE in the context of existing Ekman layer

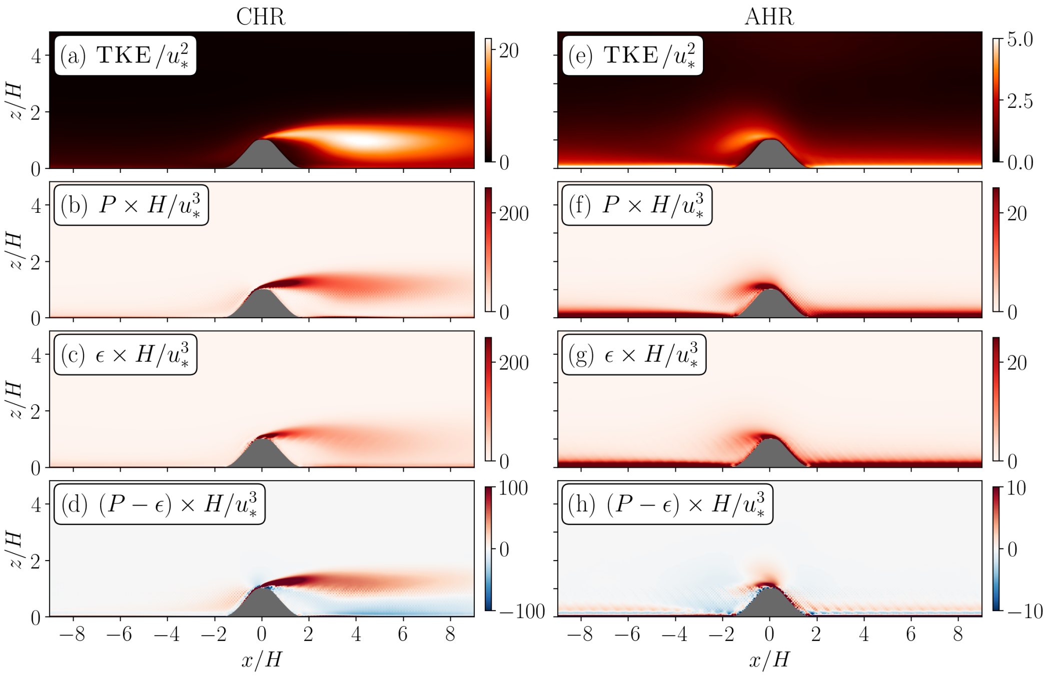

FIG. 4. TKE, production (P), dissipation (ϵ), and net transport ($P - \epsilon$) for the rotating cases. The left panels are for CHR, while the right panels are for AHR.

and topographic flow literature. As such, we consider only the net transport, grouping together its constituent terms as the difference between production and dissipation ($P - \epsilon$).

It is immediately clear from Figs. 4(a) and 4(e) that the strength of the TKE in the shear layer is roughly an order of magnitude bigger in CHR than it is in AHR. For a topography of fixed shape and no rotational influence, [24] and [50] have shown that bottom roughness and upstream shear are the two leading predictors in separation onset and intensity. While the magnitude of the far-field shear is identical between CHR and AHR (since the far field is in an Ekman balance), the component $\frac{\partial \overline{u}}{\partial z}$ is larger in CHR and is the primary contributor to separation strength, resulting in a more turbulent shear layer. As a result, the magnitudes of P and ϵ are also larger in the shear layer of CHR. The resulting deviation from the far-field P and ϵ structure persists much further downstream in CHR, as expected by the larger spatial extent of the separation bubble.

Due to the nonlocal nature of turbulent wakes, the implications for the transport of TKE differ for CHR and AHR on the basis of their differing separation strengths. This is quantified in Figs. 4(d) and 4(h). In CHR, it can be seen that the shear layer is characterized by an imbalance of the form $P > \epsilon$, where TKE is then transported in the vertical (downward) direction until it is dissipated. The AHR case is quite different, where the shear layer's maximum P is confined mostly to the region directly above the hill crest, quickly recovering to the far-field state where P and ϵ nearly balance. This balance is never reestablished in CHR due to the pronounced separation, resulting in a boundary layer with greater variations in its horizontal and vertical structures. As we will show in Sec. III B, these differences in the transport of turbulence will play a big role in shaping the velocity field, and therefore the mean transport characteristics.

Profiles of the turbulent momentum fluxes ($\overline{u'w'}$ and $\overline{v'w'}$) are shown in Figs. 5(a) and 5(d) along different positions in the domain. Note that CHR and AHR are scaled for interpretability. The peak of the shear layer's location is clear in both cases, aligned roughly with the height of the topography. The decay of the shear layer in AHR is revealed in its rapid depression of $\overline{u'w'}$ with downstream

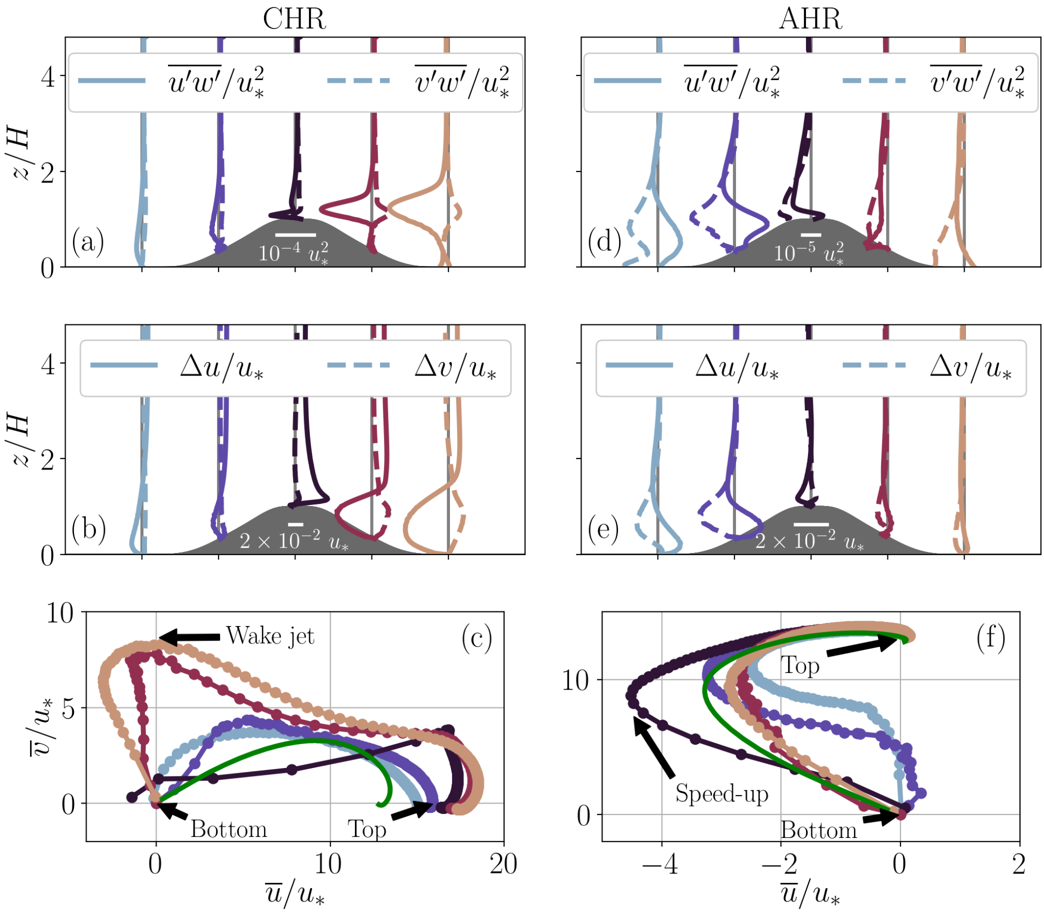

FIG. 5. Reynolds stresses (top row) velocity speedup (middle row) and hodographs (bottom row) for the rotating cases. The left panels are for CHR, while the right panels are for AHR. The vertical profiles in the bottom row are at the x/H locations corresponding to their color in the top two rows. The green line in the bottom row is from a flat-bottom simulation, with a background geostrophic current direction that is consistent with the CH and AH cases.

distance [Fig. 5(d)]. AHR also experiences near-bottom Reynolds stresses that are comparable in magnitude to the peak values, indicative of a weaker separation bubble. Conversely, CHR has peak values of $\overline{u'w'}$ that initially amplify with downstream distance, driven by the fact that the peak strength of the flow reversal in CHR occurs further downstream than it does in AHR. The relative magnitudes of the near-bottom values in CHR are minuscule when compared to the shear layer. As such, turbulent transport is highly efficient in exchanging momentum between the inner and outer regions, but decays quickly near the bottom, resulting in a separation bubble that persists with little resistance. This is consistent with Fig. 4, where the magnitude and extent of the turbulence were shown to be far greater in CHR than in AHR.

Both the topography and separation bubble impose a constraint on the flow that is often quantified by the velocity speedup, given by

$$\Delta u(z) = u(\delta z) - u_\infty(\delta z), \tag{10}$$

where $u_\infty(\delta z)$ is the unperturbed, upstream velocity a distance δz from the bottom and $u(\delta z)$ is the velocity at a height δz above the topography. This is shown for both the streamwise and spanwise components of velocity in Figs. 5(b) and 5(e). We observe a large speedup occurring in the u component of CHR directly above the crest, in line with the literature across a variety of speedup prediction methods [17]. CHR also experiences positive values of Δu above the separation bubble, whereas the spatial extent of the separation bubble in AHR is far more limited and thus does not impose the same constraint. Modulation of Δv occurs primarily in the wake of the topography in both cases. As noted in our discussion of Fig. 3, the wake magnitude of Δv in AHR is reduced, while it is magnified in CHR.

The last row of Fig. 5 more clearly shows the influence of topography on a canonical Ekman boundary layer via the hodographs. Profiles are at the x locations corresponding to the above rows of the same figure, where the green line is from a simulation with a flat bottom for comparison. The influence of topography in CHR is widespread in the sense that the velocity field assumes a larger magnitude in almost all locations above the topography. This is especially true in the wake, where values $\Delta u < 0$ due to the recirculation combine with the wake jet ($\Delta v > 0$) to create large deviations from the typical Ekman spiral near the bottom. Attenuation of the velocity field in the AHR case results in a similar effect, although here, the near-bottom deviations of the spiral are in the opposite sense, now driven by the fact that $\Delta u > 0$ and $\Delta v < 0$. Modulation of the spiral by the topography is clear near its vicinity in both cases and far downstream in the CHR case. Tracing the path of each spiral from bottom to top reveals a similar behavior across all profiles, where the velocity components near the bottom experience large deviations from the upstream profile, while the outer region is more reminiscent of a typical Ekman spiral. In other words, the near-bottom velocity is controlled by the topographic influence, while the upper boundary layer is controlled by the rotational influence. The top two rows of Fig. 5 suggest this transition occurs around $z = 2H$, though the vertical extent of the topographic influence is clearly more pronounced in CHR, evidenced by the fact none of the velocity profiles recover geostrophic balance.

Despite these near-bottom modifications, the spiraling structure of the hodographs in the last row of Fig. 5 are indicative of boundary layers that are still responding to the influence of rotation. Even near the bottom, where the hodographs display their largest deviations, the presence of both horizontal velocity components demonstrates a non-negligible effect from the Coriolis force. This may appear contradictory with the relatively high Rossby number of 30 estimated in Sec. II B, but it can be reconciled by considering an integral measure of a turbulent Ekman number ($Ek = \frac{|\nabla\cdot\overline{\boldsymbol{u}'\boldsymbol{u}'}|}{f(\overline{\boldsymbol{u}}-\boldsymbol{u}_g)}$), with $Ek \approx 1$ in both CHR and AHR when horizontally averaged. Since the near-bottom dynamics are dominated by the turbulence, the bulk Rossby number based on the exterior mean flow fails to capture the importance of rotation near the bottom. In the next section, we will analyze the transport budget to illustrate how these results modify ageostrophic transport.

B. Transport balance

We now return to the integral balance of a flat Ekman layer discussed in Sec. I [Eqs. (4) and (5)]. The definition of the Ekman transport in these equations is based on integrating over the boundary-layer height. In practice, we integrate to the top of the domain due to the turbulence being present over the entire depth. Equations (4) and (5) indicate that the boundary-layer transport is governed entirely by the magnitude and direction of the bottom stress, suggesting that the presence of other influences (e.g., pressure perturbations and advection) could lead to disruptions in the observed transport. To this end, Fig. 6 shows the vertical integral of the ageostrophic velocity ($\boldsymbol{U}_a$) and compares it against the bottom stress "prediction." The immediate takeaway is that the dynamical balance in Eqs. (4) and (5) does not hold. We treat the far-field flows to be approximately in an Ekman balance, evidenced by the fact the integrated transports approach the bottom stress predictions at the boundaries of the domain (i.e., the black line is nearly equal to the blue line).

The top row of Fig. 6 shows that the influence of topography on transport is stronger in CHR than in AHR, especially in the wake, reaching magnitudes that are nearly double the far-field magnitude. In CHR, all locations downstream from $x/H = -2$ have an integrated transport that is larger in magnitude than that from a flat Ekman layer, with positions of maxima that appear to align with the

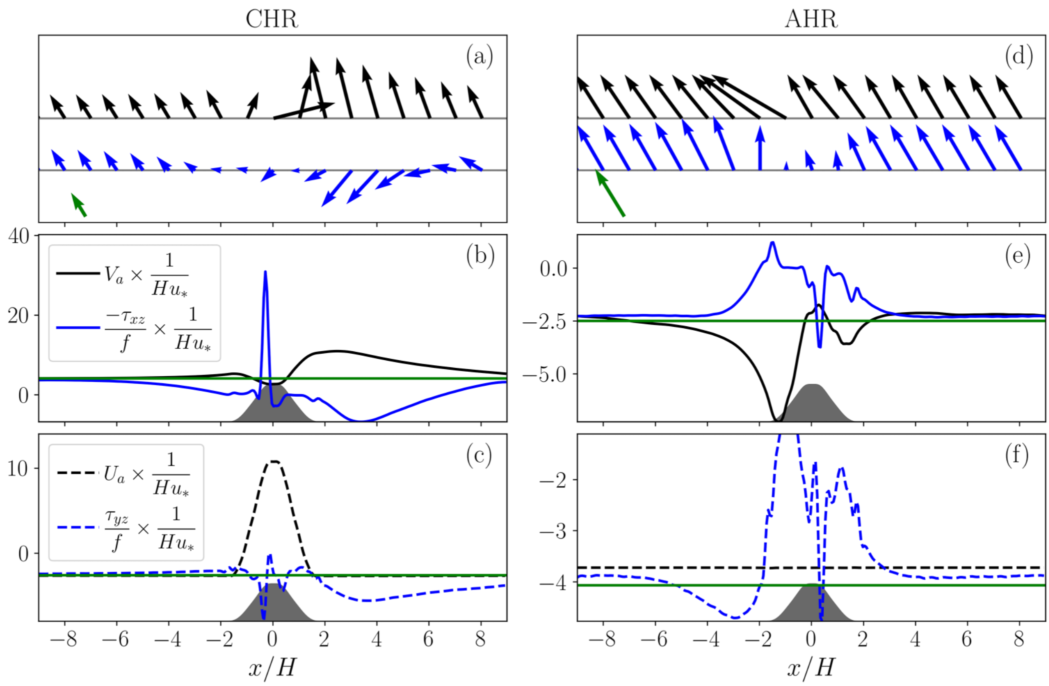

FIG. 6. Ekman transport calculated via direct integration (black) and τ/f (blue), following Eqs. (4) and (5). We integrate over the domain height as an approximation to the boundary-layer height δ (see the beginning of Sec. III B for rationale). The top row shows this in vector form, with the components of the vector being shown in the bottom two rows. The green lines and arrows are from a simulation with a flat bottom. Note that the arrows in the top row are scaled differently in CHR and AHR.

hill crest and wake-intensified jet. This is consistent with Fig. 5(c), where the increase of Δu above the hill crest and the increase of Δv in the wake drove an increase in velocity magnitude relative to the flat Ekman layer case. The wake jet's influence is apparent here in the increase of V_a [Fig. 6(b)], while the speedup is evident in U_a above the hill [Fig. 6(c)]. The fact that U_a retains the same value everywhere except in the direct vicinity of the topography is due to the requirement that the flow rate in the x direction be conserved.

AHR presents a spatial distribution of transport with maxima that occur on the upslope and downslope ends of the topography and a minimum above the crest [Fig. 6(e)]. The minimum above the hill crest is a consequence of the speedup influence on the v -component of velocity, while $U_a(x = 0)$ is shown to be identical to its far-field value [Fig. 6(f)]. Most of the changes to the integrated transport in AHR are then related to V_a. Most notably, the attenuation of v ($\Delta v < 0$) in the wake introduces large negative deviations to the transport that drives an increase in its magnitude.

The deviations from Ekman balance seen in Fig. 6 can also be identified by looking at the vertical structure of the transport anomaly. To do this, we define a horizontal transport anomaly vector, $\boldsymbol{\psi}'(x, z)$, with components of the form

$$\psi_x'(x, z') = \int_0^{z'} (\overline{v}(x, z) - v_g)dz, \tag{11}$$

$$\psi_y'(x, z') = \int_0^{z'} (\overline{u}(x, z) - u_g)dz, \tag{12}$$

where z' is free to vary from 0 to the height of the domain ($4.8H$). The subscripts x and y are chosen to match the component of the momentum balance that the right-hand sides of Eqs. (11) and (12)

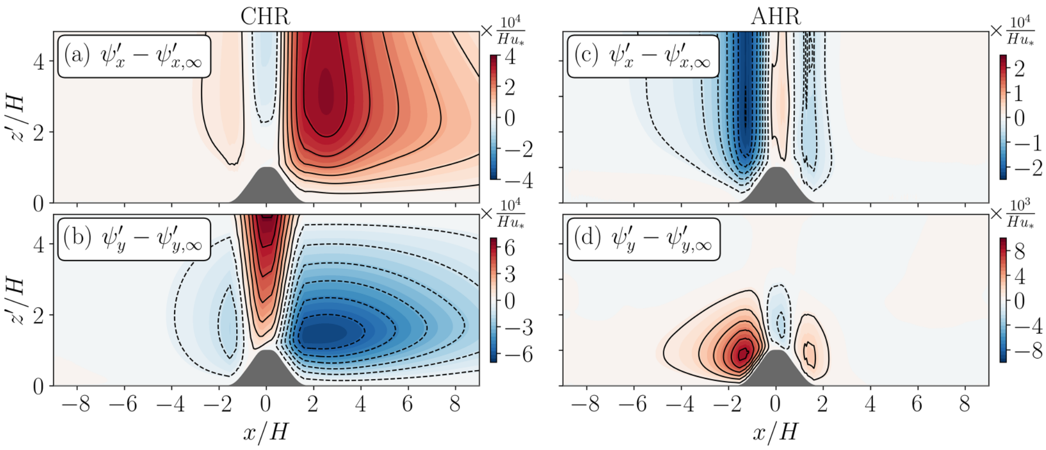

FIG. 7. Deviations of $\boldsymbol{\psi}'$ [Eqs. (11) and (12)] from its far-field value, $\boldsymbol{\psi}'_\infty$. Dashed contours indicate negative values, while solid contours indicate positive values.

contribute to [see Eq. (13)]. These expressions are identical to the integrals in Eqs. (4) and (5) when $z' = \delta$, meaning $\psi'_x(x, \delta) = V_a$ and $\psi'_y(x, \delta) = U_a$. Plotted in Fig. 7 are the deviations of $\boldsymbol{\psi}'$ from its far-field value, $\boldsymbol{\psi}'_\infty$. We subtract the two quantities as we did to calculate the velocity speedups in Eq. (10), such that the difference is always taken a distance δz from the bottom. $\boldsymbol{\psi}'_\infty$ is recognized as the transport associated with a flat-bottom case, meaning that any nonzero values observed in Fig. 7 can be understood as deviations from canonical Ekman transport.

A secondary circulation pattern is revealed in both cases, with a rotational sense of the same sign on either side of the hill. The circulation is strongly modulated by the wake, where maximum values of ψ'_y occur above the separation region in CHR and around $z = H$ in AHR [Figs. 7(c) and 7(d)]. The nonlocal influence of the topography in CHR is evident in the downstream deviation of $\boldsymbol{\psi}'$ from $\boldsymbol{\psi}'_\infty$. This is in contrast to AHR, where both components of $\boldsymbol{\psi}'$ return to their far-field values over a shorter horizontal distance. The above-crest speedup is present in both cases, appearing as a positive deviation of ψ'_y in CHR [Fig. 7(b)] and a negative deviation of ψ'_y in AHR [Fig. 7(d)]. The speedup influence is notably larger in CHR than it is in AHR, consistent with Figs. 5(b) and 5(e) and Figs. 6(c) and 6(f).

While the presence of the wake is important in both cases, the characteristics of its influence differ. In CHR, the wake jet associated with the v component of velocity introduces anomalously larger transports in the y direction, as evidenced by the large values of ψ'_x in the wake of CHR [Fig. 7(a)]. In AHR, the v component of velocity is attenuated in the wake, leading to anomalously smaller (more negative) transports in the y direction [Fig. 7(c)]. Note that in both cases, anomalies introduced by the wake persist to the top of the domain. Since $\boldsymbol{\psi}'(x, \delta) = \boldsymbol{U_a}(x)$, this can be viewed as a bulk increase in the transport anomaly, as observed in Fig. 6. ψ'_y illustrates the influence of the flow reversal associated with the u component of velocity. Specifically, the flow reversal is, by definition, in the opposite direction of the background flow, leading to anomalous ψ'_y values that are of opposite sign to the far-field value ($\psi'_{y,\infty}$).

The influence of topography on integrated transport can be summarized for the two cases as follows. In CHR, the influence of the speedup is so strong that it deflects the transport to the right of what would be observed in a flat case, simultaneously increasing its magnitude [Fig. 6(a)]. The transport direction slowly returns to its far-field orientation as the speedup effect decreases in influence. During this transition, the wake jet increases the transport magnitude further, though the direction is now almost aligned with the far field. The return to the far-field transport is finally dictated by the decay of the wake jet. In AHR, the transport deviations are entirely controlled by changes to v. In particular, attenuation of v in both the upslope and downslope regions of the topography leads to

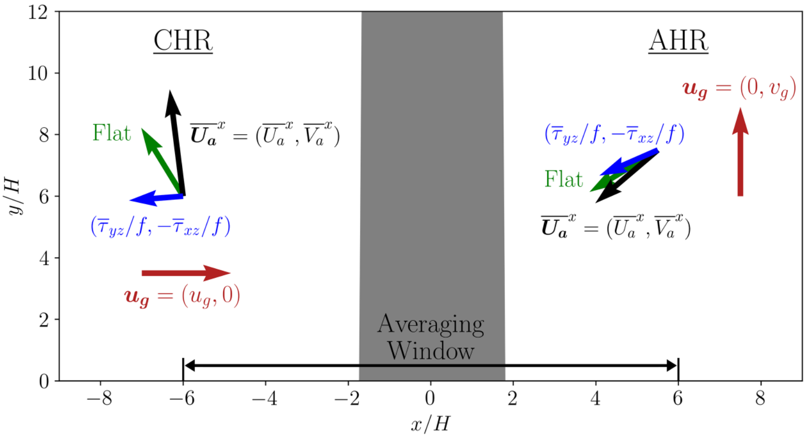

FIG. 8. Top view showing the transport direction and magnitude, averaged on the interval of $x/H = [-6, 6]$. The green arrow is from the case without topography, the black arrow is the integrated transport, and the blue arrow is the stress-predicted transport. The magnitude of the red arrow is irrelevant and is only present to indicate the direction of geostrophic flow. The (x, y) positions of all arrows in the domain are also irrelevant, as they are displaying spatial averages for the respective cases.

a transport direction that is deflected to the left of its far-field orientation [Fig. 6(d)]. While the u component of velocity does not directly introduce deviations to the integrated transport, its influence via the recirculation bubble is still important, as it is the mechanism by which v is damped in the wake. In a bulk sense, we can understand CHR's transport direction as being deflected to the right, and AHR's transport deflected to the left, both with respect to their far-field transport direction.

Bulk deflections in the transport can be seen more clearly in Fig. 8, where we plot the spatial average of the transport vector over the interval of $x/H = [-6, 6]$ (i.e., we average the integrated transport in Fig. 6 over this interval). It is interesting to note that, in both CHR and AHR, the stress-predicted transport and integrated transport are deflected in the opposite sense when compared to the flat case. Both results contribute to worsening the stress prediction based on the flat dynamics of Eqs. (4) and (5). This is largely due to the outsized role played by the pressure drag, which is an order of magnitude bigger than the bottom stress in CHR and roughly twice the magnitude of the bottom stress in AHR.

As expected, CHR experiences larger changes to the bulk transport, with a 35% increase in magnitude and a 24° change in direction relative to the flat case. In contrast, AHR only experienced a 2% increase in magnitude with a 9° change in direction. Although not shown here, an average over the topography ($x/H = [-2, 2]$) leads to a 15% increase in magnitude and a 16° change in direction for AHR, highlighting the more local nature of its dynamics.

The increase in transport in CHR has an appreciable nonlocal persistence, being in stark contrast to the more local modifications of AHR's transport. We seek to better understand these differences by analyzing the transport budget. We start by considering the relevant terms of the momentum equation for a two-dimensional problem where all variables have been separated into mean and fluctuating components:

$$\underbrace{\overline{\boldsymbol{u}} \cdot \nabla \overline{\boldsymbol{u}}}_{\text{MA}} = -\underbrace{\nabla p_a}_{\text{PGF}'} - \underbrace{\nabla \cdot \overline{\boldsymbol{u}'\boldsymbol{u}'}}_{\text{RSD}} + \underbrace{f(\overline{\boldsymbol{u}} - \boldsymbol{u}_g)}_{\text{ET}}. \tag{13}$$

From left to right, the terms are mean advection (MA), the pressure gradient force associated with pressure anomalies (PGF′), Reynolds stress divergence (RSD), and the Ekman transport (ET). Note that the subgrid-scale stress is absorbed into the Reynolds stresses and that the last term in Eq. (13) is the quantity integrated in Fig. 6, only multiplied by the Coriolis frequency, f. While

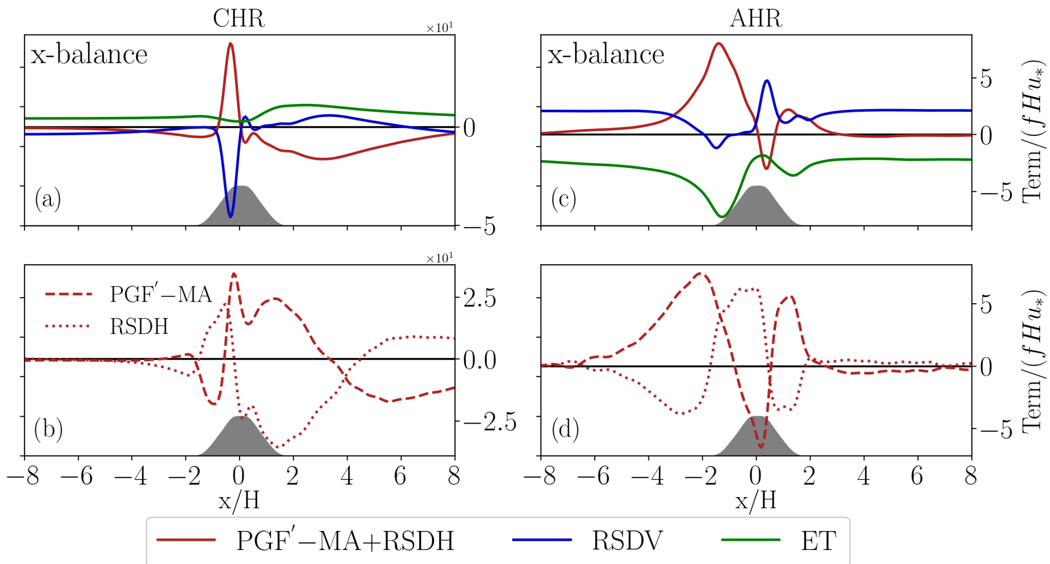

FIG. 9. Vertically integrated x-momentum budgets for the rotating cases [i.e., vertical integration of Eqs. (13) and (14) for $i = 1$]. The left panels are for CHR, while the right panels are for AHR.

we call this the Ekman transport, we recognize the dynamics here do not reflect that of the Ekman balance discussed in Sec. I. We further separate RSD into its horizontal divergences (RSDH) and vertical divergences (RSDV) as

$$\text{RSDH} = -\frac{\partial \overline{u'\boldsymbol{u}'}}{\partial x}, \tag{14}$$

$$\text{RSDV} = -\frac{\partial \overline{\boldsymbol{u}'w'}}{\partial z}, \tag{15}$$

so that RSD = RSDH + RSDV. In the above equations, we ignore terms with derivatives in the y direction due to the spatial homogeneity of the topography. This decomposition is motivated by the fact that a canonical Ekman balance consists only of contributions from RSDV, meaning that RSDH can be lumped into the category of "non-Ekman" terms. The partitioning of "Ekman" vs non-Ekman terms is done in both Figs. 9 and 10 for the x and y transport balances, respectively, achieved by vertically integrating all terms in Eq. (13). We again see an upstream balance reminiscent of an Ekman layer in both cases, where RSDV almost exactly balances the Ekman transport. The bottom rows of Figs. 9 and 10 show the decomposition of the non-Ekman terms into RSDH and the residual of PGF′ − MA.

Starting with the x balance of CHR [Fig. 9(a)], we see that the Ekman transport plays a smaller role in the overall momentum budget, but is still altered by the associated dynamics. In general, RSDV does not exhibit a canonical Ekman balance behavior in the vicinity of the topography's influence since it never achieves a balance with the Ekman transport. In the vicinity of the separating region (just before $x/H = 0$) we see a large spike in RSDV that is slightly larger in magnitude than the residual non-Ekman terms, leading to an Ekman transport that must decrease in magnitude to compensate the budget. In the center of the wake, we see that RSDH > PGF′ − MA [Fig. 9(b)], suggesting that the wake jet is partially linked to a horizontal divergence of the streamwise velocity variance. Further downstream, this switches so that PGF′ − MA ∼ RSDV > RSDH, leading to a persistence of anomalously large Ekman transport (as seen in Figs. 7 and 6).

AHR is, in general, slightly more complicated due to the apparent variety of dynamical regimes seen in Fig. 9(c). On the upstream slope ($x/H > 0$), PGF′ and MA serve to increase the Ekman

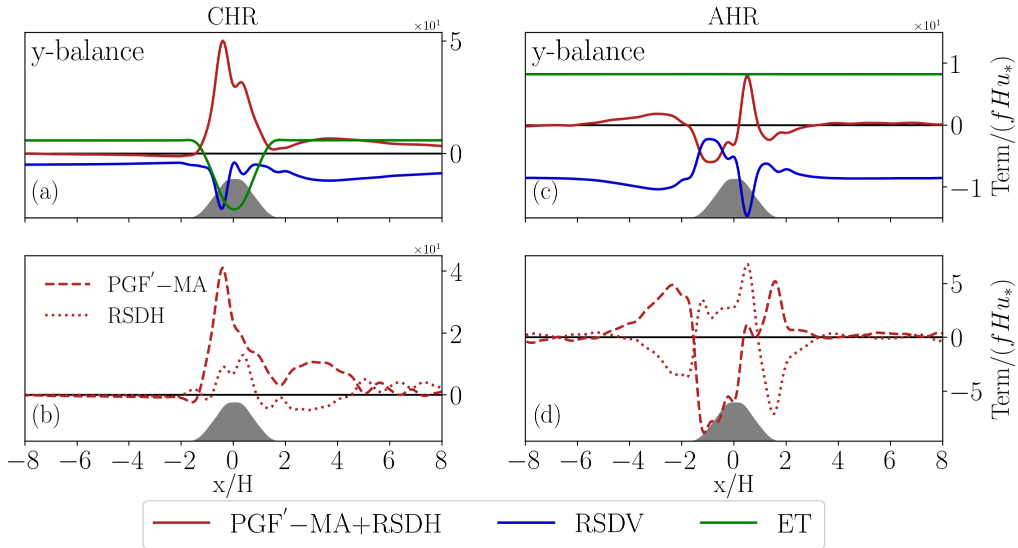

FIG. 10. Vertically integrated y-momentum budgets for the rotating cases [i.e., vertical integration of Eqs. (13) and (14) for $i = 2$]. The left panels are for CHR, while the right panels are for AHR. We note that there is no mean PGF′ anomaly in the y direction, so here, PGF′ = 0.

transport while RSDH serves to decrease it [Fig. 9(c)]. RSDV is mostly unchanged until reaching the point of separation, albeit with a far smaller spike when compared to that of CHR. RSDV in AHR acts to increase the transport magnitude above the crest, although is overcome by the non-Ekman terms. In particular, PGF′ − MA > RSDH above the crest [Fig. 9(d)]. In the center of the wake of AHR ($-2 < x/H < -1$), the sum of the non-Ekman terms combine to maximize the Ekman transport (note that this corresponds to a *decrease* in the spanwise velocity). Thereafter, the return to an Ekman balance is governed by the decay of RSDH and PGF′ − MA. It is interesting to note that in AHR, changes to the Ekman transport appear to be anticorrelated with RSDV, much more so than is evident in CHR.

Changes to the Ekman transport observed in Fig. 9 can also be understood via the y balance, as changes to the v component of velocity are governed principally by the dynamics in this direction. We then look to Fig. 10, noting that PGF′ = 0 here due to the homogeneity associated with the topography being two-dimensional. For CHR, the primary takeaway is that the wake is characterized by a negative MA that drives values of RSDV that are roughly twice its far-field value. Higher values of RSDV then promote entrainment of anomalously high v velocity, consistent with the changes to the Ekman transport observed in Figs. 7–9. In general, RSDH is less important in the y balance of CHR than it was in the x balance. This is in contrast to AHR, where RSDH appears to have a stronger influence on RSDV than MA in the upslope region. In the wake, this switches so that MA is the primary mechanism by which RSDV decreases. These decreases in RSDV on the slopes of AHR then lead to an attenuation of v. Following Eq. (11), this results in an increase in the Ekman transport.

IV. SUMMARY AND CONCLUSIONS

We sought to understand the influence of topography on the typical structure of a flat-bottom Ekman layer, with particular attention given to a steeply sloping two-dimensional ridge. We found that the topography introduced large deviations from canonical Ekman balance such that Eqs. (4) and (5) are not satisfied. The nature of the deviations depended greatly on the orientation of the background current with respect to the topography. In the case where the geostrophic current was aligned perpendicular to the ridge axis (CHR, $\boldsymbol{u}_g = (u_g, 0)$), we observed a strongly separating flow with far downstream influence. Conversely, when the geostrophic current was aligned with the ridge axis (AHR, $\boldsymbol{u}_g = (0, v_g)$), flow separation was much weaker, allowing the system to recover a canonical Ekman balance more rapidly. In both cases, flow separation appears to preclude the possibility of a local bottom-stress transport prediction, as the reversal in flow direction drives a bottom stress that is inconsistent with the magnitude and direction of the transport overlying the separation bubble.

In both cases, the topography strongly impacts the mean flow and turbulence in the lower portion of the boundary layer (up to $z = 2H$), above which the flow tends to approach the traditional Ekman balance. In the cross-hill direction (u), the effects of the topography are driven by the modified pressure field and are thus very similar to the nonrotating case, characterized by a speedup above the hill and recirculation downstream. The along-hill direction of the flow (v), however, is greatly modified near the bottom, with a strong jet developing within the recirculation region for CHR and a slowdown of the background flow in AHR. Interestingly, this makes AHR's wake reminiscent of nonrotating cases where the upstream flow is at an angle with the topography (see [51], where the spanwise component is reported to reverse in direction). The dependence of the spanwise velocity structure appears to have a sensitive relationship with the strength of the shear layer and the nature of the background flow, warranting more research in the context of rotation.

These results suggest that transport in the ocean's bottom boundary layer may depend greatly on small-scale topography. Both CHR and AHR experienced increases in the transport to the left of the mean flow, with the near-bottom modulation of the along-hill velocity playing an essential role. For example, the transport magnitude in CHR is most impacted by the along-hill wake jet and is driven by large contributions from mean advection and the horizontal divergence of the Reynolds stresses. Conversely, the weaker wake turbulence in AHR results in the along-hill component of velocity being attenuated in the wake. Quantification of the bulk transport (Fig. 8) shows that these changes have substantial far-field influence in CHR, while being more localized to the topography in AHR.

The complicated nature of realistic seafloor geometry and background current orientation implies there is a spectrum of complexity lying between the cases presented here. While our simulations focus on cases with flow separation, there is literature that shows the structure of Ekman layers can be modified even over gentle slopes [49]. Nevertheless, many of the differences between CHR and AHR appear to be linked to the strength of separation. With nonrotating dynamics studies illustrating a high sensitivity to the topographic slope [24,25], there is a clear indication that such a study in the present formulation would be insightful. Lastly, the omission of density stratification is only applicable to regions of the ocean that have well-mixed water columns. A simulation study of flat-bottom Ekman layers showed that the boundary-layer transport is relatively insensitive to the strength of stratification [10], although further research is warranted on how stratification may influence a topographically modulated bottom Ekman boundary layer.

ACKNOWLEDGMENTS

The research leading to these results was funded by the ARPA-E MARINER Program DE-AR0000920. We would like to acknowledge high-performance computing support from the Derecho system (Grant doi: 10.5065/qx9a-pg09) provided by the NSF National Center for Atmospheric Research (NCAR), sponsored by the National Science Foundation.

[1] V. W. Ekman, On the influence of the earth's rotation on ocean-currents, Ark. Mat. Astron. Fys. **2**, 1 (1905).

[2] J. Deardorff, A three-dimensional numerical investigation of the idealized planetary boundary layer, Geophys. Fluid Dyn. **1**, 377 (1970).

[3] G. N. Coleman, J. H. Ferziger, and P. R. Spalart, A numerical study of the turbulent Ekman layer, J. Fluid Mech. **213**, 313 (1990).

[4] E. Deusebio, G. Brethouwer, P. Schlatter, and E. Lindborg, A numerical study of the unstratified and stratified Ekman layer, J. Fluid Mech. **755**, 672 (2014).

[5] R. G. Williams and M. J. Follows, The Ekman transfer of nutrients and maintenance of new production over the North Atlantic, Deep Sea Res. Part I **45**, 461 (1998).

[6] J. Yang, The seasonal variability of the arctic ocean Ekman transport and its role in the mixed layer heat and salt fluxes, J. Clim. **19**, 5366 (2006).

[7] B. Chen, D. Yang, C. Meneveau, and M. Chamecki, Numerical study of the effects of chemical dispersant on oil transport from an idealized underwater blowout, Phys. Rev. Fluids **3**, 083801 (2018).

[8] Y. Yoshikawa, T. Endoh, T. Matsuno, T. Wagawa, E. Tsutsumi, H. Yoshimura, and Y. Morii, Turbulent bottom Ekman boundary layer measured over a continental shelf, Geophys. Res. Lett. **37**, L15605 (2010).

[9] A. Perlin, J. N. Moum, J. M. Klymak, M. D. Levine, T. Boyd, and P. M. Kosro, Organization of stratification, turbulence, and veering in bottom Ekman layers, J. Geophys. Res.: Oceans **112**, C05S90 (2007).

[10] J. R. Taylor and S. Sarkar, Stratification effects in a bottom Ekman layer, J. Phys. Oceanogr. **38**, 2535 (2008).

[11] A. Schaeffer, M. Roughan, and J. E. Wood, Observed bottom boundary layer transport and uplift on the continental shelf adjacent to a western boundary current, J. Geophys. Res.: Oceans **119**, 4922 (2014).

[12] A. Schaeffer, M. Roughan, and B. D. Morris, Cross-shelf dynamics in a Western Boundary Current regime: Implications for upwelling, J. Phys. Oceanogr. **43**, 1042 (2013).

[13] N. Malan, M. Roughan, G. J. Stanley, R. Holmes, and J. Li, Quantifying cross-shelf transport in the east Australian Current System: A budget-based approach, J. Phys. Oceanogr. **52**, 2555 (2022).

[14] P. S. Jackson and J. C. R. Hunt, Turbulent wind flow over a low hill, Q. J. R. Meteorol. Soc. **101**, 929 (1975).

[15] J. C. R. Hunt, S. Leibovich, and K. J. Richards, Turbulent shear flows over low hills, Q. J. R. Meteorol. Soc. **114**, 1435 (1988).

[16] F. T. Smith, P. W. M. Brighton, P. S. Jackson, and J. C. R. Hunt, On boundary-layer flow past two-dimensional obstacles, J. Fluid Mech. **113**, 123 (1981).

[17] A. A. S. Pirooz and R. G. J. Flay, Comparison of speed-up over hills derived from wind-tunnel experiments, wind-loading standards, and numerical modelling, Boundary Layer Meteorol. **168**, 213 (2018).

[18] A. J. Bowen, The prediction of mean wind speed above simple 2D hill shapes, J. Wind Eng. Ind. Aerodyn. **15**, 259 (1983).

[19] F. Hewer, Non-linear numerical model predictions of flow over an isolated hill of moderate slope, Boundary Layer Meteorol. **87**, 381 (1998).

[20] R. L. Simpson, J. H. Strickland, and P. W. Barr, Features of a separating turbulent boundary layer in the vicinity of separation, J. Fluid Mech. **79**, 553 (1977).

[21] P. R. Spalart and J. H. Watmuff, Experimental and numerical study of a turbulent boundary layer with pressure gradients, J. Fluid Mech. **249**, 337 (1993).

[22] Y. Na and P. Moin, Direct numerical simulation of a separated turbulent boundary layer, J. Fluid Mech. **374**, 379 (1998).

[23] Z. Yang and P. R. Voke, Large-eddy simulation of boundary-layer separation and transition at a change of surface curvature, J. Fluid Mech. **439**, 305 (2001).

[24] N. Wood, The onset of separation in neutral, turbulent flow over hills, Boundary Layer Meteorol. **76**, 137 (1995).

[25] S. Cao and T. Tamura, Experimental study on roughness effects on turbulent boundary layer flow over a two-dimensional steep hill, J. Wind Eng. Ind. Aerodyn. **94**, 1 (2006).

[26] G. P. Almeida, D. F. G. Durao, and M. V. Heitor, Wake flows behind two-dimensional model hills, Exp. Therm. Fluid Sci. **7**, 87 (1993).

[27] H. Ólafsson and P. Bougeault, The effect of rotation and surface friction on orographic drag, J. Atmos. Sci. **54**, 193 (1997).

[28] H. Wells, S. Webster, and A. Brown, The effect of rotation on the pressure drag force produced by flow around long mountain ridges, Q. J. R. Meteorol. Soc. **131**, 1321 (2005).
[29] H. A. Khaledi, M. Barri, and H. I. Andersson, On the stabilizing effect of the Coriolis force on the turbulent wake of a normal flat plate, Phys. Fluids **21**, 095104 (2009).
[30] M. Barri and H. I. Andersson, Turbulent flow over a backward-facing step. Part 1. Effects of anti-cyclonic system rotation, J. Fluid Mech. **665**, 382 (2010).
[31] S. Frei, E. Burman, and E. Johnson, Attached and separated rotating flow over a finite height ridge, Phys. Rev. Fluids **9**, 084801 (2024).
[32] M. Abkar and F. Porté-Agel, Influence of the Coriolis force on the structure and evolution of wind turbine wakes, Phys. Rev. Fluids **1**, 063701 (2016).
[33] T. Zhou and T. Ishihara, Numerical investigation of neutral atmospheric boundary layer flows over flat terrain and three-dimensional hills considering the effects of Coriolis force, J. Wind Eng. Ind. Aerodyn. **240**, 105482 (2023).
[34] E. Bou-Zeid, C. Meneveau, and M. Parlange, A scale-dependent Lagrangian dynamic model for large eddy simulation of complex turbulent flows, Phys. Fluids **17**, 025105 (2005).
[35] R. Mittal and G. Iaccarino, Immersed boundary method, Annu. Rev. Fluid Mech. **37**, 239 (2005).
[36] B. Chen and M. Chamecki, Turbulent kinetic energy budgets over gentle topography covered by forests, J. Atmos. Sci. **80**, 91 (2023).
[37] B. Fornberg, *A Practical Guide to Pseudospectral Methods 1* (Cambridge University Press, Cambridge, UK, 1998).
[38] Q. Li, E. Bou-Zeid, and W. Anderson, The impact and treatment of the Gibbs phenomenon in immersed boundary method simulations of momentum and scalar transport, J. Comput. Phys. **310**, 237 (2016).
[39] M. Heisel, B. Chen, J. F. Kok, and M. Chamecki, Gentle topography increases vertical transport of coarse dust by orders of magnitude, J. Geophys. Res.: Atmos. **126**, e2021JD034564 (2021).
[40] J. Fröhlich, C. P. Mellen, W. Rodi, L. Temmerman, and M. A. Leschziner, Highly resolved large-eddy simulation of separated flow in a channel with streamwise periodic constrictions, J. Fluid Mech. **526**, 19 (2005).
[41] F. Feddersen, E. L. Gallagher, R. T. Guza, and S. Elgar, The drag coefficient, bottom roughness, and wave-breaking in the nearshore, Coastal Eng. **48**, 189 (2003).
[42] S. S. Zilitinkevich, On the determination of the height of the Ekman boundary layer, Boundary Layer Meteorol. **3**, 141 (1972).
[43] P. K. Kundu, I. M. Cohen, and D. R. Dowling, *Fluid Mechanics* (Academic, New York, 2015).
[44] R. J. Stevens, J. Graham, and C. Meneveau, A concurrent precursor inflow method for Large Eddy Simulations and applications to finite length wind farms, Renewable Energy **68**, 46 (2014).
[45] W. Anderson, J. M. Barros, K. T. Christensen, and A. Awasthi, Numerical and experimental study of mechanisms responsible for turbulent secondary flows in boundary layer flows over spanwise heterogeneous roughness, J. Fluid Mech. **768**, 316 (2015).
[46] H. G. Hwang and J. H. Lee, Secondary flows in turbulent boundary layers over longitudinal surface roughness, Phys. Rev. Fluids **3**, 014608 (2018).
[47] A. K. Blackadar, Boundary layer wind maxima and their significance for the growth of nocturnal inversions, Bull. Am. Meteorol. Soc. **38**, 283 (1957).
[48] B. J. H. V. d. Wiel, A. F. Moene, G. J. Steeneveld, P. Baas, F. C. Bosveld, and A. A. M. Holtslag, A conceptual view on inertial oscillations and nocturnal low-level jets, J. Atmos. Sci. **67**, 2679 (2010).
[49] A. Shapiro, E. Fedorovich, and S. Rahimi, A unified theory for the great plains nocturnal low-level jet, J. Atmos. Sci. **73**, 3037 (2016).
[50] S. Cao, T. Wang, Y. Ge, and Y. Tamura, Numerical study on turbulent boundary layers over two-dimensional hills — Effects of surface roughness and slope, J. Wind Eng. Ind. Aerodyn. **104–106**, 342 (2012), in 13th International Conference on Wind Engineering.
[51] Z. Liu, J. Cao, B. Yan, Y. Wang, and H. Wang, Study of wind-direction effects on flow fields over two-dimensional hills using Large Eddy Simulations, J. Wind Eng. Ind. Aerodyn. **204**, 104285 (2020).